Supplementary Information: "Coherent two-dimensional terahertz-terahertz-Raman spectroscopy"

Ian A. Finneran,[1] Ralph Welsch,[1] Marco A. Allodi,[1,*]
Thomas F. Miller III,[1] and Geoffrey A. Blake[1,2,†]
[1]*Division of Chemistry & Chemical Engineering,*
California Institute of Technology, Pasadena, California 91125, USA
[2]*Division of Geological & Planetary Sciences,*
California Institute of Technology, Pasadena, California 91125, USA

(Dated: May 25, 2016)

I. EXPERIMENTAL SETUP

A schematic of the 2D-TTR experiment is shown in Fig. S1(a). As outlined in the Methods section of the main text, the heart of the system is a 38 fs Coherent Legend Elite USP Ti:Sa regenerative amplifier seeded by a 80 MHz Coherent Mantis oscillator. The 3.6 mJ, 800 nm pulses from the amplifier are sent into an optical parametric amplifier (OPA, Light Conversion Ltd) and downconverted to 1450 nm (signal, 500 μJ) and 1780 nm (idler, 330 μJ). The OPA signal beam is routed through a second delay line (t_1, Fig. S1(a)) and used to drive a 3 mm aperture DSTMS (4-N,N-dimethylamino-4-N-methyl-stilbazolium 2,4,6-trimethylbenzenesulfonate) THz generation crystal (Rainbow Photonics). The OPA idler output is sent directly to a second 3 mm aperture DSTMS crystal. The DSTMS crystals are optimized for THz generation phase matching near 1450 nm, but we achieve a roughly equivalent THz power near 1700 nm. The 1450 nm signal/1780 nm OPA setting was chosen to optimize the THz power of both beams, taking into account the wavelength dependent conversion efficiency of the OPA and the DSTMS efficiency.

The two separate THz pulses (3 mm beam diameter) from the signal and idler OPA beams are combined on a knife edge prism mirror, and residual optical light is blocked with a thin layer of black polyethylene and a roughened TOPAS plate. The THz pulses are run through a Gaussian telescope with 7.5× magnification (22.5 mm THz beam diameter) and then focused onto the sample with a 2 inch Effective Focal Length (EFL) 90 degree off axis parabolic mirror. Both pulses have a peak field strength of $\sim$300 kV/cm at the sample. Liquids are held in a 1 mm path length Suprasil quartz cuvette. The transient birefringence in the sample is probed with a small portion of the 800 nm light (1 mW) that is split off from the amplifier and sent down a mechanical delay line (t_2, Fig. S1(a)). As described in our previous work, we have implemented heterodyne detection of the transient birefringence using a 10^5:1 optical polarizer, an 800 nm $\lambda/4$ plate, a Wollaston prism, and a pair of silicon photodiodes[1]. No nonlinear signal was detected from the empty quartz cuvette.

To isolate the two-pulse 2D-TTR signal we chop the signal beam at $f_{rep}/6$ and the idler beam at $f_{rep}/4$, where $f_{rep} = 1$ kHz, the repetition rate of the laser. We detect the birefringence on a lock in amplifier at $f_{rep}/12$=83.3 Hz. The 1 pulse rejection of the experiment on CS_2 is shown in Fig. S2(a). When either the signal or idler is blocked there is no detectable interference from the single pulse signals, confirming that the experiment is

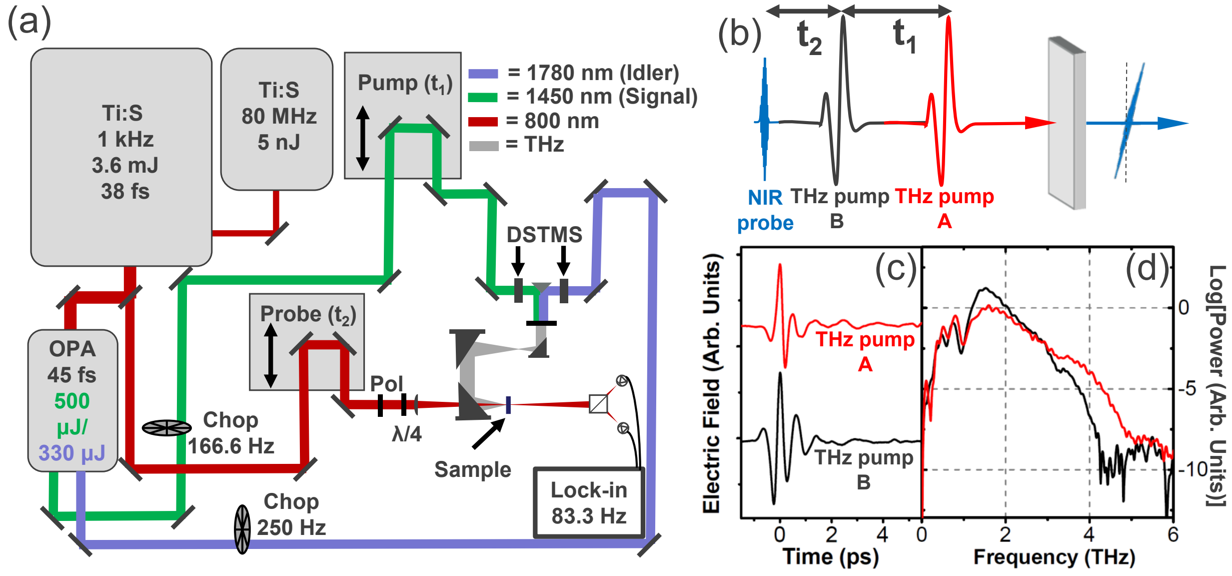

FIG. S1. (a) A diagram of the 2D-TTR experiment. See text for details. (b) The pulse sequence used in 2D-TTR spectroscopy. (c) The measured time domain traces of the THz pulses using electro-optic sampling in a 200 micron thick GaP crystal. (d) The FFTs of the traces shown in (c).

exclusively sensitive to the two pulse signal. Next, we measured the single pulse signals and compared their intensity with the two pulse signal (Fig. S2(b)). The two pulse signal is 2× stronger than the idler response and 4× stronger than the signal response.

The THz fields from both the signal- and idler-driven DSTMS emitters were measured with electro-optic detection using a 200 micron thick GaP crystal placed at the sample position (Fig. S1(c)). The bandwidth of the signal pulse extends from 0.5-5 THz, while that from the idler extends over 0.5-4 THz. The polarization purity of the THz pulses were measured with a wiregrid polarizer and a Gentec-EO inc. QS3-IL broadband pyroelectric detector mounted in a QS-I-TEST box at the sample position. The signal THz pulse has a polarization purity of 80%, while the idler THz pulse has a polarization purity of 90%. Finally, the peak field strength of both THz fields are ∼300 kV/cm measured with the same pyroelectric detector and the EO traces. The details of the THz field strength measurement are given in our previous work[1].

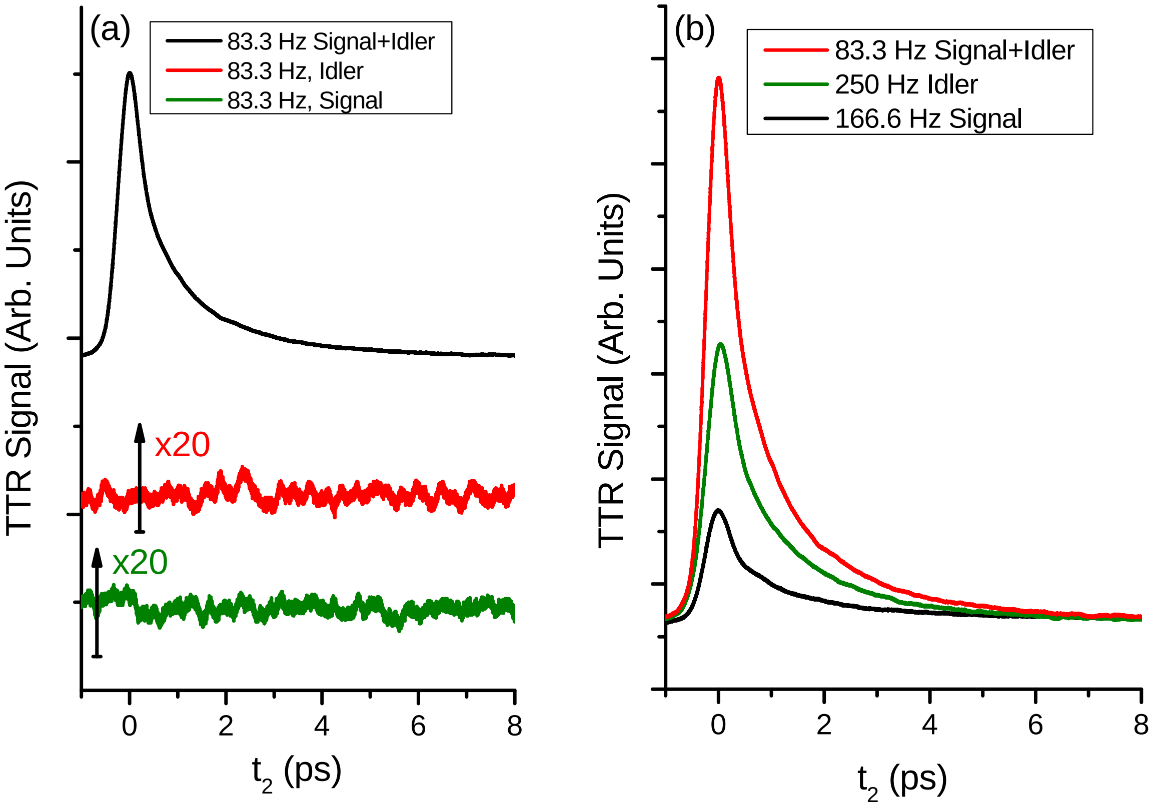

FIG. S2. (a) The measured single pulse rejection of the 2D-TTR experiment. No interference from single pulse signals could be detected. (b) The 2- and 1-pulse responses of liquid CS_2. The 2-pulse signal is stronger than either 1-pulse response.

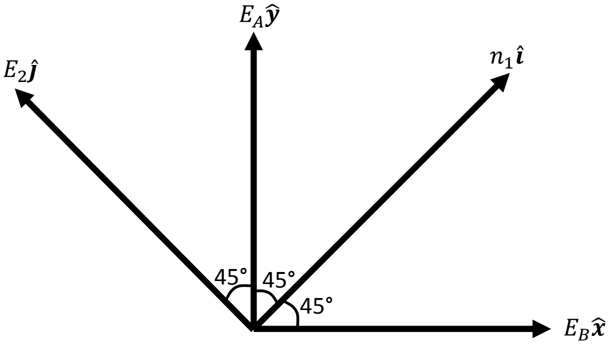

FIG. S3. Polarization directions relevant to the 2D-TTR experiment.

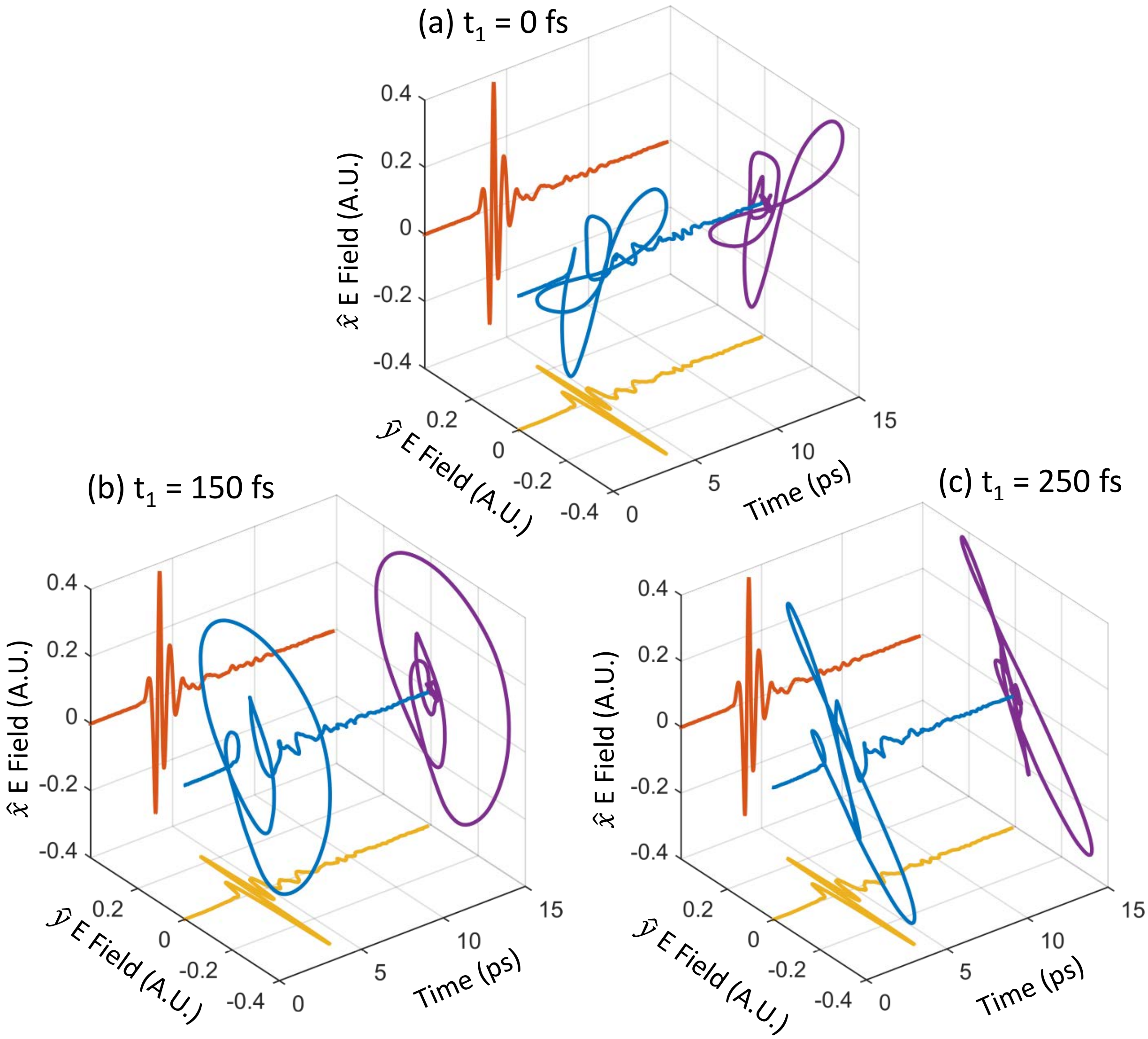
(a) t_1 = 0 fs

(b) t_1 = 150 fs

(c) t_1 = 250 fs

FIG. S4. Time domain traces of the total THz electric field, including polarization at (a) t_1=0 fs, (b) t_1=150 fs, and (c) t_1=250 fs.

II. ORIENTATIONAL MODEL

A schematic of the light polarizations used in the 2D-TTR experiment is shown in Fig. S3. THz pulse A is polarized vertically, or along the $\hat{y}$ unit vector, while THz pulse b is polarized horizontally, or along the $\hat{x}$ unit vector. When the THz pulses are overlapped in time, the polarization of the total field is dependent on t_1. For example, at $t_1 = 0$ fs the field is rotated roughly toward the $\hat{i}$ direction (Fig. S4(a)), while at t_1=250 fs the $\hat{j}$ direction (Fig. S4(c)). At t_1=150 fs the field is roughly circular, with equal components along the $\hat{\imath}$ and $\hat{\jmath}$ directions (Fig. S4(b)). The NIR probe pulse is oriented along the $\hat{y}$ direction and the balanced detection is sensitive to the difference in the change of refractive index oriented along $\hat{\imath}$ (n_1) and along $\hat{\jmath}$ (n_2): $S \propto \Delta n(t) = n_1(t) - n_2(t)$. In the absence of an excitation field in an isotropic liquid $n_1 = n_2$ so $\Delta n = 0$. When a THz pulse is applied in the $\hat{\imath}$ direction, this leads to a signal given by

$$\Delta n_i(t) = \int d\mathrm{t}_2 R(\mathrm{t}_2) E_1^2(t - \mathrm{t}_2), \tag{1}$$

where R is the response function of the liquid and E_1 is the field oriented in the $\hat{\imath}$ direction. For an isotropic medium, excitation along the $\hat{\jmath}$ direction causes a sign change in Δn

$$\Delta n_j(t) = -\int d\mathrm{t}_2 R(\mathrm{t}_2) E_2^2(t - \mathrm{t}_2), \tag{2}$$

where E_2 is the field oriented in the $\hat{\jmath}$ direction. The total signal is thus

$$\Delta n_{tot}(t) = \Delta n_i(t) + \Delta n_j(t). \tag{3}$$

The total THz field is given by $E_{tot} = E_\mathrm{A}\hat{x} + E_\mathrm{B}\hat{y}$. Alternatively, we can express this in the $\hat{\imath}$, $\hat{\jmath}$ coordinate system

$$E_{tot} = \frac{\sqrt{2}}{2}(E_\mathrm{A} + E_\mathrm{B})\hat{\imath} + \frac{\sqrt{2}}{2}(E_\mathrm{B} - E_\mathrm{A})\hat{\jmath} = E_1\hat{\imath} + E_2\hat{\jmath}, \tag{4}$$

$$\Delta n_{tot}(t) = \int d\mathrm{t}_2 R(\mathrm{t}_2) E_1^2(t - \mathrm{t}_2) - \int d\mathrm{t}_2 R(\mathrm{t}_2) E_2^2(t - \mathrm{t}_2). \tag{5}$$

Plugging in our values for E_1 and E_2 we get (for a given value of t_1)

$$\Delta n_{tot}(t) = 2\int d\mathrm{t}_2 R(\mathrm{t}_2) E_\mathrm{A}(t - \mathrm{t}_2) E_\mathrm{B}(t - \mathrm{t}_2). \tag{6}$$

Now, using the model from our previous work we break the response function into two components: an instantaneous electronic response and a single exponential orientational response[1]. We use the measured electric fields to calculate the electronic portion of the signal, or

$$S_e(\mathrm{t}_1, \mathrm{t}_2) = E_\mathrm{A}(\mathrm{t}_2 + \mathrm{t}_1) E_\mathrm{B}(\mathrm{t}_2). \tag{7}$$

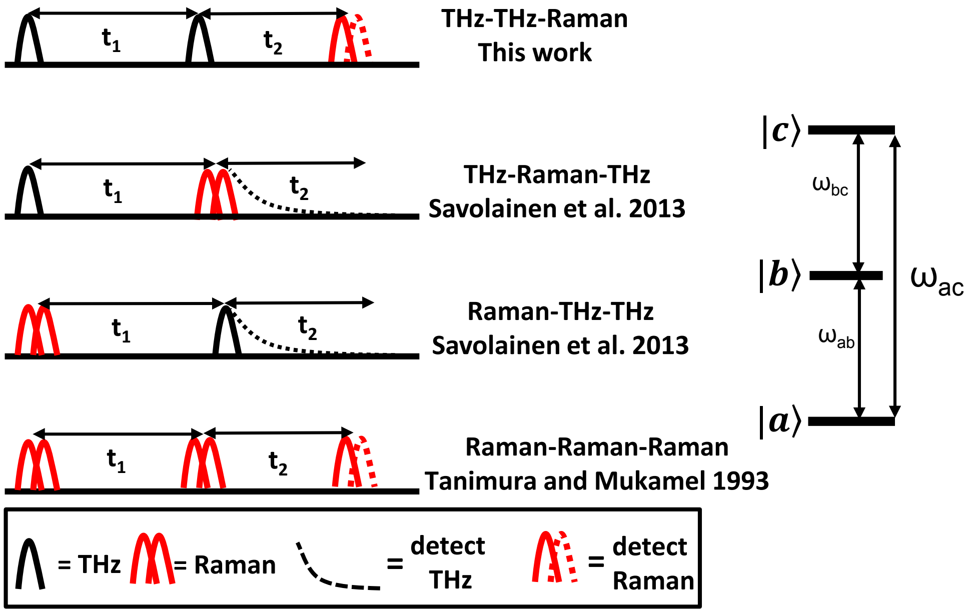

FIG. S5. A comparison of the various 2D pulse sequences that have been used to study low energy modes of liquids via interactions with a three level system[2–4]. The signals from these techniques provide different information and are thus complementary[5].

We then calculate the orientational portion of the signal, S_o, with the discrete time step equation

$$S_o(\mathrm{t}_1, \mathrm{t}_2 + \Delta\mathrm{t}_2) = S_o(t) + [E_\mathrm{A}(\mathrm{t}_2 + \Delta\mathrm{t}_2 + \mathrm{t}_1)E_\mathrm{B}(\mathrm{t}_2 + \Delta\mathrm{t}_2) - S_o(\mathrm{t}_2)/\tau]\Delta\mathrm{t}_2, \tag{8}$$

where τ is the orientational decay constant[1].

III. PERTURBATIVE DENSITY MATRIX DERIVATION

For the 2D-TTR experiment we have two THz pulses followed by one Raman pulse. If we assume a third order interaction (the leading order contribution) this limits us to signals that originate from the interaction of light with a three-level system (triad) and at least one transition that is forbidden in the harmonic representation (Fig. S5). To understand the measured signals we start with the nonlinear polarization [6, 7]

$$P^{(3)}(t) = \iint d\mathrm{t}_1 d\mathrm{t}_2\, R^{(3)}(\mathrm{t}_1, \mathrm{t}_2) E_\mathrm{B}(t - \mathrm{t}_2) E_\mathrm{A}(t - \mathrm{t}_1 - \mathrm{t}_2) E_\mathrm{nir}(t), \tag{9}$$

and the third order response function [6, 7]

$$R^{(3)}(\mathrm{t}_1,\mathrm{t}_2) = -\frac{1}{\hbar^2} tr\langle \Pi(\mathrm{t}_1+\mathrm{t}_2)[\mu(\mathrm{t}_1)[\mu(0),\rho_{\mathrm{eq}}]]\rangle \quad . \tag{10}$$

where ρ_{eq} is the equilibrium density matrix. Expanding commutators yields:

$$\begin{aligned} R^{(3)}(\mathrm{t}_1,\mathrm{t}_2) =& -\frac{1}{\hbar^2} tr\langle \Pi(\mathrm{t}_1+\mathrm{t}_2)\mu(\mathrm{t}_1)\mu(0)\rho_{\mathrm{eq}} - \Pi(\mathrm{t}_1+\mathrm{t}_2)\mu(\mathrm{t}_1)\rho_{\mathrm{eq}}\mu(0) \\ & + \Pi(\mathrm{t}_1+\mathrm{t}_2)\rho_{\mathrm{eq}}\mu(0)\mu(\mathrm{t}_1) - \Pi(\mathrm{t}_1+\mathrm{t}_2)\mu(0)\rho_{\mathrm{eq}}\mu(\mathrm{t}_1)\rangle. \end{aligned} \tag{11}$$

For shorthand, we now designate $\Pi(\mathrm{t}_1+\mathrm{t}_2)$ as Π, $\mu(0)$ as μ_0, and $\mu(\mathrm{t}_1)$ as μ_1. Any TTR signal must come from one of four interactions

$$tr\langle \Pi\mu_1\mu_0\rho_{\mathrm{eq}}\rangle; \quad tr\langle \Pi\mu_1\rho_{\mathrm{eq}}\mu_0\rangle; \quad tr\langle \Pi\rho_{\mathrm{eq}}\mu_0\mu_1\rangle; \quad tr\langle \Pi\mu_0\rho_{\mathrm{eq}}\mu_1\rangle. \tag{12}$$

This leads to 24 possible interactions plus their complex conjugates, all of which are shown in Fig. S6 with double-sided Feynman diagrams. From this point forward, we will, by convention, only consider the 24 terms in Fig. S6 and not their complex conjugates, as the conjugate terms do not carry any extra information. Adding the 24 terms together yields 12 distinct terms plus their complex conjugates:

$$\begin{aligned} R^{(3)}(\mathrm{t}_1,\mathrm{t}_2) \propto & \mu_{ab}\mu_{bc}\Pi_{ac}((\rho_{bb}-\rho_{aa})e^{-i\omega_{ab}\mathrm{t}_1}e^{-i\omega_{ac}\mathrm{t}_2} - (\rho_{cc}-\rho_{bb})e^{-i\omega_{bc}\mathrm{t}_1}e^{-i\omega_{ac}\mathrm{t}_2}) \\ & + \mu_{ac}\mu_{bc}\Pi_{ab}(\rho_{cc}-\rho_{aa})e^{-i\omega_{ac}\mathrm{t}_1}e^{-i\omega_{ab}\mathrm{t}_2} - \mu_{ab}\mu_{ac}\Pi_{bc}(\rho_{bb}-\rho_{aa})e^{-i\omega_{ab}\mathrm{t}_1}e^{+i\omega_{bc}\mathrm{t}_2} \\ & + \mu_{bc}\mu_{ac}\Pi_{ab}(\rho_{cc}-\rho_{bb})e^{-i\omega_{bc}\mathrm{t}_1}e^{+i\omega_{ab}\mathrm{t}_2} - \mu_{ac}\mu_{ab}\Pi_{cb}(\rho_{cc}-\rho_{aa})e^{-i\omega_{ac}\mathrm{t}_1}e^{-i\omega_{bc}\mathrm{t}_2} + c.c. \end{aligned} \tag{13}$$

where ρ_{xx} is a diagonal entry in the equilibrium density matrix corresponding to the population of state x. We now define the population, p_x, and population difference, p_{xy},

$$\rho_{xx} = p_x, \quad p_{xy} = p_y - p_x, \tag{14}$$

and plug these in the response function:

$$\begin{aligned} R^{(3)}(\mathrm{t}_1,\mathrm{t}_2) \propto & \mu_{ab}\mu_{bc}\Pi_{ac}(p_{ab}e^{-i\omega_{ab}\mathrm{t}_1}e^{-i\omega_{ac}\mathrm{t}_2} - p_{bc}e^{-i\omega_{bc}\mathrm{t}_1}e^{-i\omega_{ac}\mathrm{t}_2}) \\ & + \mu_{ac}\mu_{bc}\Pi_{ab}p_{ac}e^{-i\omega_{ac}\mathrm{t}_1}e^{-i\omega_{ab}\mathrm{t}_2} - \mu_{ab}\mu_{ac}\Pi_{bc}p_{ab}e^{-i\omega_{ab}\mathrm{t}_1}e^{+i\omega_{bc}\mathrm{t}_2} \\ & + \mu_{bc}\mu_{ac}\Pi_{ab}p_{bc}e^{-i\omega_{bc}\mathrm{t}_1}e^{+i\omega_{ab}\mathrm{t}_2} - \mu_{ac}\mu_{ab}\Pi_{cb}p_{ac}e^{-i\omega_{ac}\mathrm{t}_1}e^{-i\omega_{bc}\mathrm{t}_2} + c.c. \end{aligned} \tag{15}$$

The THz pulses used in this work have a modest bandwidth of 0.5-4.0 THz. This is less than the lowest energy vibration in all three molecules studied. Thus, the THz light contains sufficient bandwidth to excite ω_{ab} and ω_{bc}, but not ω_{ac}. Including this assumption, hereafter called assumption (i), we are left with

$$R^{(3)}(\mathrm{t}_1,\mathrm{t}_2) \propto \mu_{ab}\mu_{bc}\Pi_{ac}(p_{ab}e^{-i\omega_{ab}\mathrm{t}_1}e^{-i\omega_{ac}\mathrm{t}_2} - p_{bc}e^{-i\omega_{bc}\mathrm{t}_1}e^{-i\omega_{ac}\mathrm{t}_2}) + c.c. \tag{16}$$

2D-TTR spectra for these interactions are shown in Fig. S7. With assumption (i) we expect two non-rephasing off-diagonal peaks for each triad, while with no assumptions we expect 4 non-rephasing and 2 rephasing peaks.

If we assume a very small angle between the two THz beams, we can determine the direction of various Liouville pathways from the Feynman diagrams. In this geometry, all three beams are in the same plane and the angle between $\vec{k}_A$ and $\vec{k}_B$ is bisected by $\vec{k}_{nir}$. For the 8 pathways observed in this work, the direction of the nonlinear signal is $\vec{k}_A + \vec{k}_B + \vec{k}_{nir}$ and $-\vec{k}_A - \vec{k}_B + \vec{k}_{nir}$. If we assume $|\vec{k}_A| = |\vec{k}_B|$ then these signals will be collinear with $\vec{k}_{nir}$. For the 16 remaining Liouville pathways this is not the case. They will have directions given by $\vec{k}_A - \vec{k}_B + \vec{k}_{nir}$ and $-\vec{k}_A + \vec{k}_B + \vec{k}_{nir}$. These signals would be slightly offset from $\vec{k}_{nir}$. However, due to the high divergence of THz light, the two THz beams will be nearly collinear at the sample and these various signals will overlap with $\vec{k}_{nir}$.

IV. SYMMETRY ANALYSIS

Using group-theoretical arguments, one can show that for any transition dipole matrix element to be non-zero, the following must be true

$$\langle \Psi_a | \widehat{\mu} | \Psi_b \rangle \neq 0 \Leftrightarrow \Gamma_a \otimes \Gamma_\mu \otimes \Gamma_b \supset A_1,$$

where Ψ_j are vibrational eigenstates, $\widehat{\mu}$ is the dipole operator, Γ_i denotes the irreducible representation of these and A_1 refers to the totally symmetric representation. In the following, this identity will be used to analyze which transitions in $\mathrm{CBr_2Cl_2}$ are forbidden in the isolated molecule limit. The point group of $\mathrm{CBr_2Cl_2}$ is C_{2v}, for which the irreducible representations of the dipole operator are A_1, B_1 and B_2. As in C_{2v} all elements are their own inverse, the direct product of the irreducible representations of any two vibrational states must also be A_1, B_1 or B_2 to give a non-zero transition probability. Consequently, for any two vibrational states where the direct product of the irreducible representations is A_2, there will be zero transition probability. This is the case when the two vibrational states under consideration transform according to A_1 and A_2 or B_1 and B_2, respectively. Thus, e.g., the transition between $|01000\rangle$ and $|00010\rangle$ is forbidden.

The same analysis can be done for CCl_4 and $CHBr_3$, but none of the transitions between the excited states considered in this work are forbidden.

V. REDUCED DENSITY MATRIX (RDM) SIMULATION

A reduced density matrix approach [6, 7] is used to qualitatively simulate the 2D-TTR spectra. The time evolution of the reduced density matrix $\boldsymbol{\rho}$ is given by the Liouville-Von Neumann equation

$$i\hbar\frac{\partial\boldsymbol{\rho}}{\partial t} = \left[\boldsymbol{H}, \boldsymbol{\rho}\right], \tag{17}$$

where $\boldsymbol{H}$ is the matrix representation of the Hamilton operator of the system under consideration. In this work, the time evolution is numerically calculated using a second-order differencing technique [8]

$$\boldsymbol{\rho}\left(t+\Delta t\right) = \boldsymbol{\rho}\left(t\right) - \frac{i}{\hbar}\ \left[\boldsymbol{H}\left(t\right), \rho\left(t\right)\right]\ 2\ \Delta t - 2\boldsymbol{\Gamma}\ \Delta t, \tag{18}$$

where $\Gamma_{i,j} = (1-\delta_{i,j})\frac{1}{\tau_{i,j}}$ defines the off diagonal decay to phenomenologically incorporate dephasing caused by the surrounding bath with an associated time-scale, $\tau_{i,j}$[6, 7].

The time-dependent Hamiltonian $\boldsymbol{H}\left(t\right)$ can be split into a time-independent Hamiltonian $\boldsymbol{H}^0$ describing the n-level system under consideration and a time-dependent Hamiltonian $\boldsymbol{H}^L(t)$ describing the interaction of the system with the two THz pulses

$$H^0_{i,j} = E_i\delta_{i,j}, \tag{19}$$

$$H^L_{i,j}(t) = \mu_{i,j}F(t), \tag{20}$$

where E_i is the energy of the i-th system eigenstate, $\mu_{i,j}$ is the transition dipole moment between state i and j and the time-dependent laser field $F(t)$ is given as

$$F(t) = A\sum_{i=1,2}\mathrm{e}^{\frac{-(t-\tau_i)^2}{2\sigma_i^2}}\cos(\omega_i(t-\tau_i)), \tag{21}$$

where τ_i, σ_i, and ω_i are the center, the width, and the frequency of the i-th laser pulse, respectively and A denotes the global field strength.

The final molecular polarizability (see Eq. (1) of the main text) is calculated as

$$P(t) = \boldsymbol{tr}\left(\boldsymbol{D}\ \boldsymbol{\rho}(t)\right) - \sum_{j=1,2} \boldsymbol{tr}\left(\boldsymbol{D}\boldsymbol{\rho_j}(t)\right), \tag{22}$$

where the matrix $\boldsymbol{D}$ contains transition probabilities for the final Raman interaction and $\boldsymbol{\rho}_j(t)$ was propagated under the influence of the j-th laser field only. The last term cancels any contributions from first-order interactions to the molecular polarizability. The final spectrum is obtained by fixing one of the THz laser pulses at $\tau_1 = 0.0$ fs. This laser pulse is used to define the experimentally controlled delay times $\mathrm{t}_1 = -\tau_2$ and $\mathrm{t}_2 = t$. Frequency-domain spectra are then obtained applying the same Fourier transform that is used to process the experimental data. To avoid problems with overlapping laser pulses, only values of $\tau_2 > \sigma_1$ are chosen. This is reasonable as the experimental spectra with the same constraints are very similar to the full experimental spectra (see Fig. S8), but exhibit lower signal-to-noise ratio and resolution.

The initial density matrix is thermally populated with a temperature of 300 K and then propagated from time t_s to time t_e. Eigenstate energies of the systems under consideration are taken from linear measurements (Fig. S9, [9–11]), and the energies of overtones are taken by summing the respective contributions, e.g. the energy of a doubly excited state is twice the energy of the singly excited state. The relative transition dipole moments are chosen to reproduce the experimental measurements and all IR transitions between states with more than 4 THz energy difference are forbidden. All other numerical values chosen are summarized in Tables S1 - S3.

VI. ANALYSIS OF EXPERIMENTAL AND RDM SIMULATED SPECTRA FOR DIBROMODICHLOROMETHANE

In this section, the robustness of the simulated CBr_2Cl_2 spectrum is investigated by studying a set of different coupling patterns. The experimental spectrum is shown in Fig. S10(a), while several simulated spectra are shown in Fig. S10(b-f). First, we will consider the case where the ν_4 and ν_5 states are only coupled to the ν_3 state. As detailed in Sec. IV of the SI, the coupling of the ν_3 state to the ν_5 state can be excluded due to their

$CHBr_3$		CCl_4		CBr_2Cl_2	
State	E	State	E	State	E
$\vert 00\rangle$, A_1	0.0	$\vert 00\rangle$, A_1	0.0	$\vert 00000\rangle$, A_1	0.0
$\vert 10\rangle$, E	4.76	$\vert 10\rangle$, E	6.51	$\vert 10000\rangle$, A_1	4.62
$\vert 01\rangle$, A_1	6.68	$\vert 01\rangle$, F_2	9.29	$\vert 01000\rangle$, A_2	5.25
$\vert 20\rangle$, $A_1 + A_2 + E$	9.52	$\vert 20\rangle$, $A_1 + A_2 + E$	13.0	$\vert 00100\rangle$, B_1	6.87
—	—	—	—	$\vert 00010\rangle$, A_1	7.25
—	—	—	—	$\vert 00001\rangle$, B_2	7.85
—	—	—	—	$\vert 20000\rangle$, A_1	9.24
—	—	—	—	$\vert 11000\rangle$, A_2	9.86
—	—	—	—	$\vert 02000\rangle$, A_1	10.5

TABLE S1. Eigenstate energies used in the calculations, in THz. (Fig. S9, [9–11]) The notation is taken from the main text and symmetry labels are given for all states.

$CHBr_3$				CCl_4				CBr_2Cl_2			
i, j	$\boldsymbol{\mu}_{i,j}$	i,j	$\boldsymbol{D}_{i,j}$	i, j	$\boldsymbol{\mu}_{i,j}$	i,j	$\boldsymbol{D}_{i,j}$	i, j	$\boldsymbol{\mu}_{i,j}$	i,j	$\boldsymbol{D}_{i,j}$
$\vert 10\rangle$, $\vert 01\rangle$	0.01	$\vert 00\rangle$, $\vert 10\rangle$	1.0	$\vert 10\rangle$, $\vert 01\rangle$	0.01	$\vert 00\rangle$, $\vert 10\rangle$	1.0	$\vert 10000\rangle$, $\vert 00100\rangle$	0.01	$\vert 00000\rangle$, $\vert 10000\rangle$	1.0
$\vert 01\rangle$, $\vert 02\rangle$	0.01	$\vert 00\rangle$, $\vert 01\rangle$	1.0	$\vert 01\rangle$, $\vert 02\rangle$	0.01	$\vert 00\rangle$, $\vert 01\rangle$	1.0	$\vert 01000\rangle$, $\vert 00100\rangle$	0.01	$\vert 00000\rangle$, $\vert 01000\rangle$	0.5
—	—	$\vert 10\rangle$, $\vert 20\rangle$	1.0	—	—	$\vert 10\rangle$, $\vert 20\rangle$	1.0	$\vert 00100\rangle$, $\vert 20000\rangle$	0.01	$\vert 00000\rangle$, $\vert 00100\rangle$	1.0
—	—	—	—	—	—	—	—	$\vert 00100\rangle$, $\vert 11000\rangle$	0.01	$\vert 00000\rangle$, $\vert 00010\rangle$	1.0
—	—	—	—	—	—	—	—	$\vert 00100\rangle$, $\vert 02000\rangle$	0.01	$\vert 00000\rangle$, $\vert 00001\rangle$	1.0
—	—	—	—	—	—	—	—	—	—	$\vert 10000\rangle$, $\vert 20000\rangle$	1.0
—	—	—	—	—	—	—	—	—	—	$\vert 10000\rangle$, $\vert 11000\rangle$	0.5
—	—	—	—	—	—	—	—	—	—	$\vert 01000\rangle$, $\vert 11000\rangle$	1.0
—	—	—	—	—	—	—	—	—	—	$\vert 01000\rangle$, $\vert 02000\rangle$	0.5

TABLE S2. Non-zero matrix elements for the dipole transition matrices, in Debye.

symmetry, which leaves coupling between the ν_4 and the ν_5 states. In panel (c) of Fig. S10 the simulated spectrum for this coupling pattern is shown. There is only one peak observed in this spectrum, which roughly matches the position of the experimentally observed double peak at (4.9 THz, 3.1 THz) and (4.9 THz, 2.5 THz). However, the four other experimentally

τ_1 in fs	0.0
τ_2 in fs	-300 – -2000
$\Delta\tau_2$ in fs	50
σ_1 in fs	250
σ_2 in fs	250
ω_1 in THz	3.0
ω_2 in THz	2.5
A in MV/cm	0.3
$\tau_{i,j}$ in fs	1500
t_s in fs	-4000
t_e in fs	4000
Δt in fs	1.0

TABLE S3. Summary of general parameters used in the density matrix propagation.

observed peaks are completely missing in this spectrum. It should be noted that ignoring any symmetry arguments and allowing coupling of the ν_3 and ν_5 states also results in a spectrum qualitatively different from the experimentally observed spectrum (see Fig. S10(e)). In this case, three major peaks are visible in the simulated spectrum. While the peak at (4.9 THz, 2.8 THz) matches one of the experimentally observed peaks, both peaks along f_2=5.2 THz do not match the experimentally observed peaks. Furthermore, the relative intensities between the peaks along f_2=4.9 THz and f_2=5.2 THz is inverted for this coupling pattern, as compared to the experimental results.

Next, the case where the ν_4 and ν_5 states are only coupled to the ν_9 state is investigated (Fig. S10(d)). In this spectrum, three peaks are visible. However, their positions along the f_1 axis do not match the experimental peaks well, and three peaks are missing completely.

Finally, in Fig. S10(f) a calculated spectrum is obtained allowing full coupling of the ν_4 and ν_5 states to the ν_3, ν_7 and ν_9 states. While this spectrum is closer to the experimentally measured one than the three cases before, several deviations can be seen. First, the experimental spectrum shows a double peak at (4.9 THz, 3.1 THz) and (4.9 THz, 2.5 THz), where the simulated spectrum only shows a single, extended peak. This peak is also shifted towards larger f_1 values compared to the double peak in the experimental spectrum. Second, the experimentally observed peak around (4.9 THz, 1.9 THz) is split into two peaks which occur with a very low intensity. Third, there are only two peaks visible in the theoretical spectrum at f_2=5.2 THz, while experimentally three peaks are observed along f_2=5.2 THz. Furthermore, the positions of the peaks in the calculated spectrum along the f_1 axis do not match the experimental peaks.

Thus, based on this analysis the most plausible explanation is that the ν_4 and ν_5 states are most strongly coupled to the ν_7 state (Fig. S10(b)). More thorough and quantitative analysis of the couplings between the vibrational states in liquid CBr_2Cl_2 is desirable; this is beyond the scope of this work and is left for future investigation.

---

* Current address: Department of Chemistry, The Institute for Biophysical Dynamics, and The James Franck Institute, The University of Chicago, Chicago, Illinois 60637, USA

† gab@gps.caltech.edu

[1] Allodi MA, Finneran IA, Blake GA (2015) Nonlinear terahertz coherent excitation of vibrational modes of liquids. *J Chem Phys* 143(23):234204.

[2] Savolainen J, Ahmed S, Hamm P (2013) Two-dimensional Raman-terahertz spectroscopy of water. *Proc Natl Acad Sci* 110(51):20402–20407.

[3] Tanimura Y, Mukamel S (1993) Two-dimensional femtosecond vibrational spectroscopy of liquids. *J Chem Phys* 99(12):9496–9511.

[4] Tokmakoff A et al. (1997) Two-dimensional Raman spectroscopy of vibrational interactions in liquids. *Phys Rev Lett* 79(14):2702.

[5] Ikeda T, Ito H, Tanimura Y (2015) Analysis of 2D THz-Raman spectroscopy using a non-markovian brownian oscillator model with nonlinear system-bath interactions. *J Chem Phys* 142(21):212421.

[6] Mukamel S (1999) *Principles of Nonlinear Optical Spectroscopy.* (Oxford University Press) No. 6.

[7] Hamm P, Zanni M (2011) *Concepts and methods of 2D infrared spectroscopy.* (Cambridge University Press).

[8] Leforestier C et al. (1991) A comparison of different propagation schemes for the time dependent Schrödinger equation. *J Comput Phys* 94(1):59 – 80.

[9] Flanders B, Cheville R, Grischkowsky D, Scherer N (1996) Pulsed terahertz transmission spectroscopy of liquid $CHCl_3$, CCl_4, and their mixtures. *J Phys Chem* 100(29):11824–11835.

[10] Shimanouchi T (1972) Tables of molecular vibrational frequencies consolidated. volume I, (DTIC Document), Technical report.

[11] Huynh T, Anderson A (1997) Infrared and raman study of solid dibromodichloromethane. *J Raman Spectrosc* 28(5):373–377.

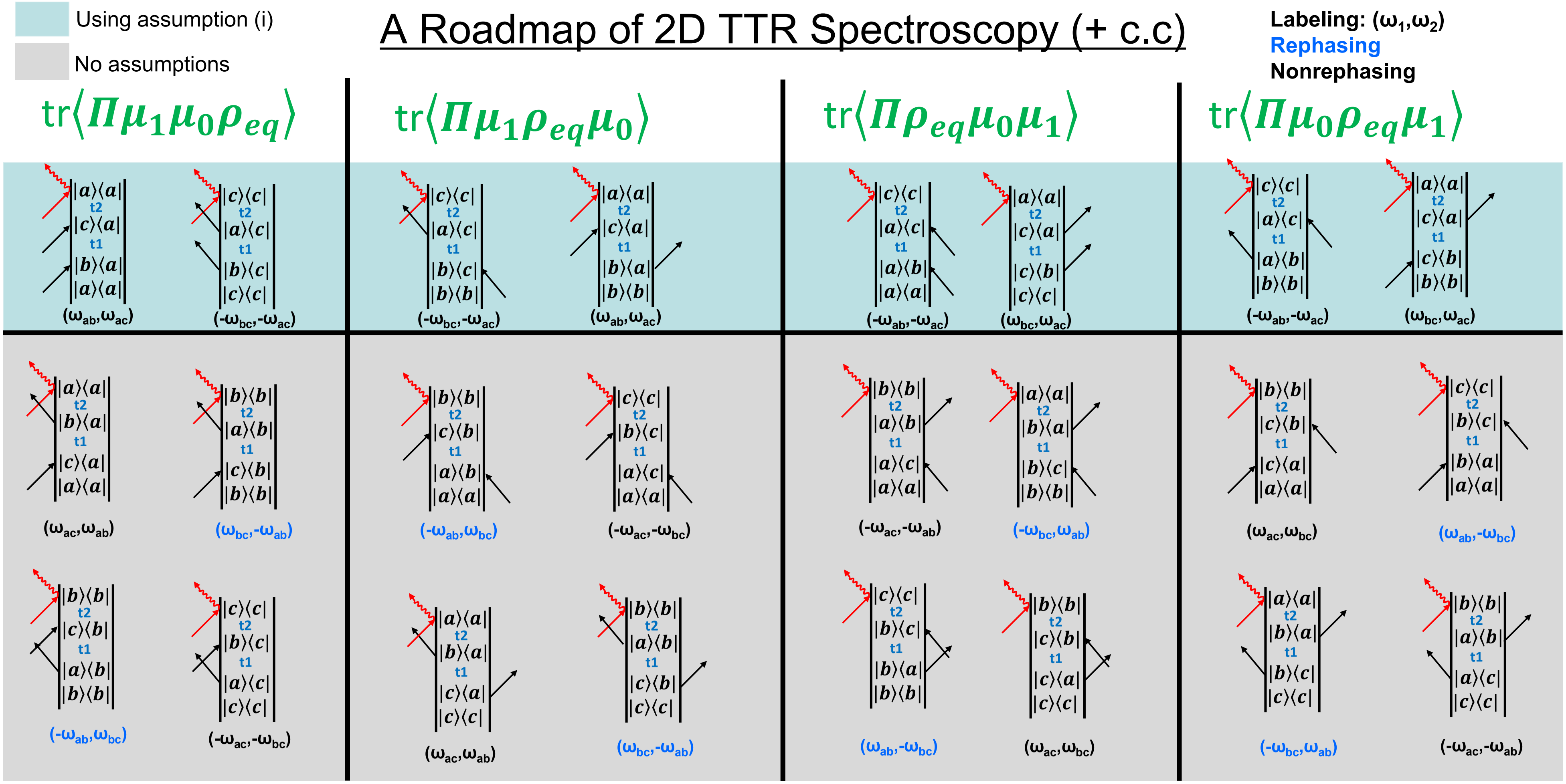

FIG. S6. Possible third-order interactions in 2D-TTR spectroscopy.

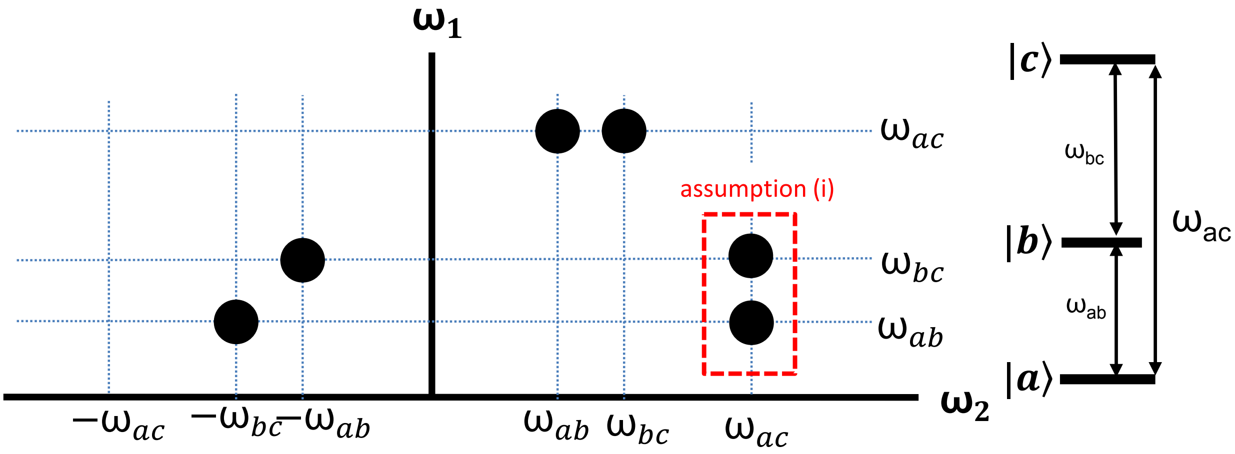

FIG. S7. The 2D-TTR spectra possible in the interaction with a three-level system.

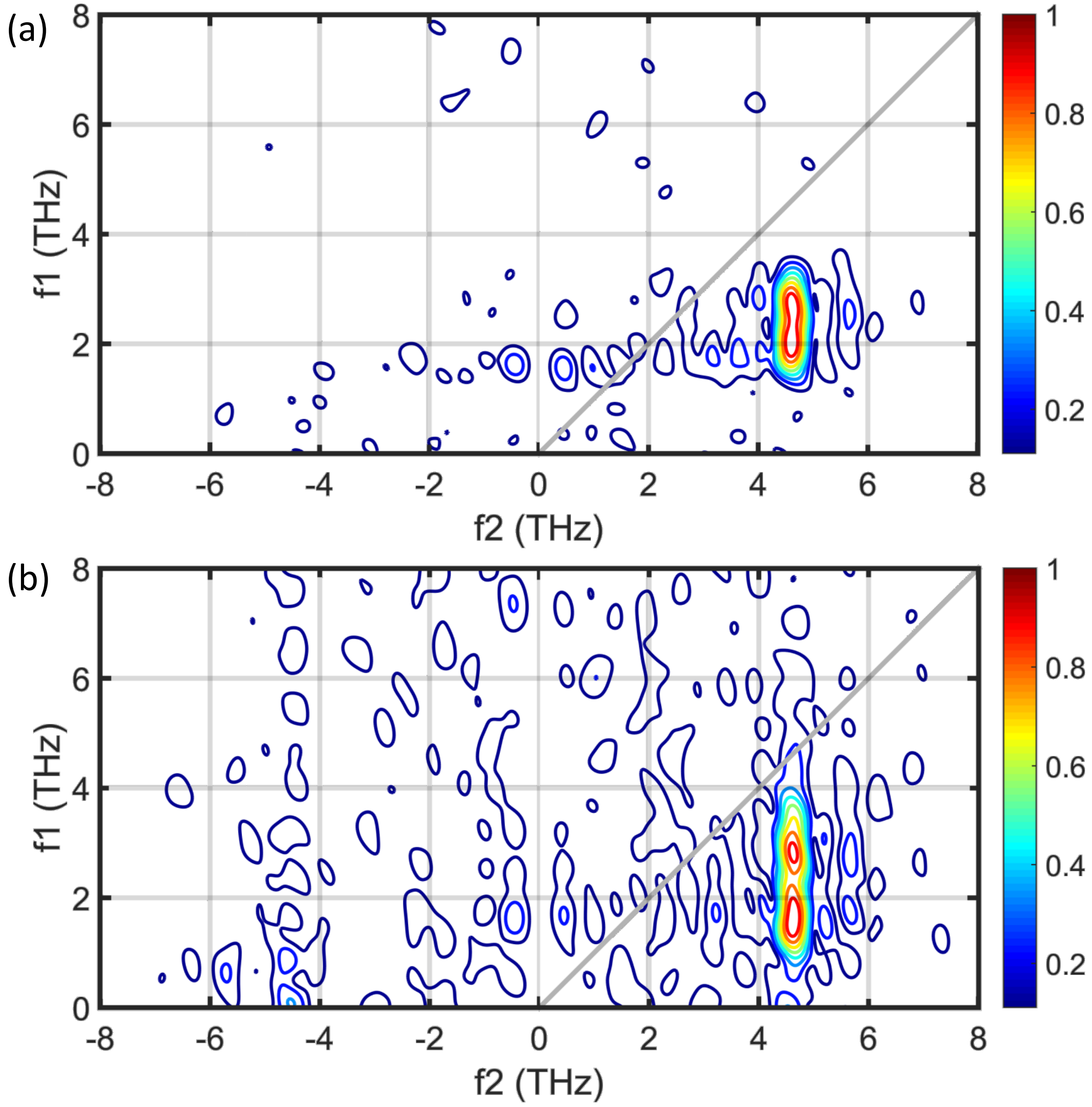

FIG. S8. (a) The 2D-TTR spectrum of bromoform, with time domain data acquired from -0.85 ps $< t_1 <$ 1.55 ps. (b) The 2D-TTR spectrum of bromoform, here the time window is 0.3 ps $< t_1 <$ 1.55 ps. The resolution and sensitivity are accordingly lower, but the doublet is still present.

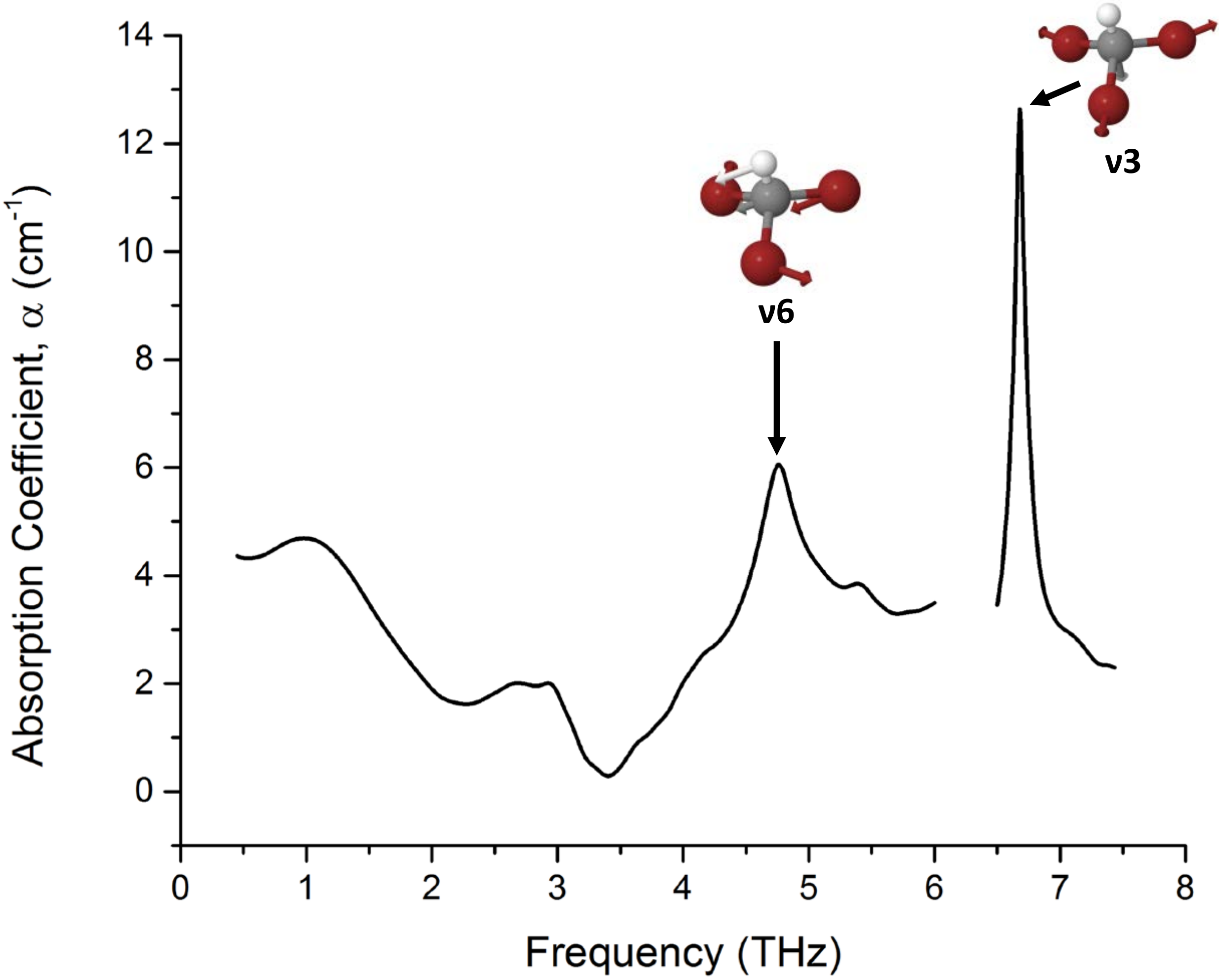

FIG. S9. The linear spectrum of bromoform, taken with a plasma filamentation THz source, and a 200 micron thick GaP crystal for EO detection.

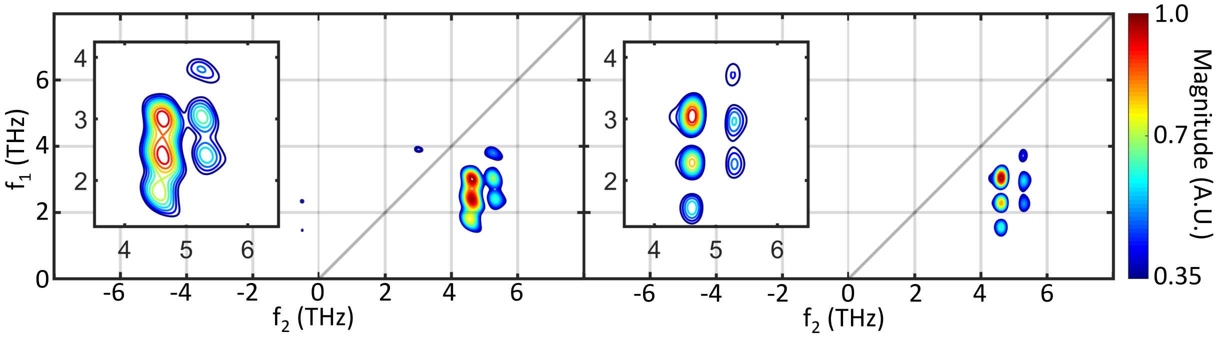

(a) Experiment

(b) RDM $v7$ coupling

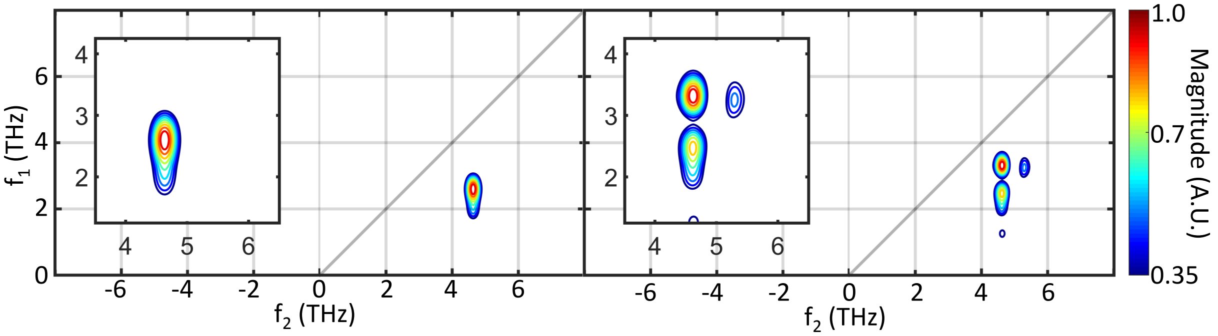

(c) RDM $v3$ coupling – with symmetry

(d) RDM $v9$ coupling

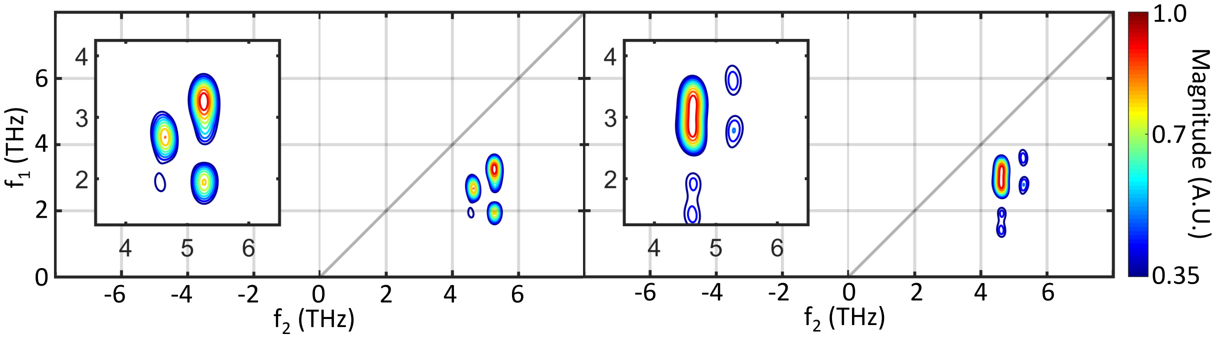

(e) RDM $v3$ coupling – no symmetry

(f) RDM $v7, v9, v3$ coupling

FIG. S10. The experimental and RDM simulated spectra for various couplings in CBr_2Cl_2.